ARTICLES
https://doi.org/10.1038/s41567-022-01527-w
nature physics

Coherent control of a multi-qubit dark state in waveguide quantum electrodynamics

Maximilian Zanner[1,2]✉, Tuure Orell[3], Christian M. F. Schneider[1,2], Romain Albert[1,2], Stefan Oleschko[1,2], Mathieu L. Juan[4], Matti Silveri[3] and Gerhard Kirchmair[1,2]

Superconducting qubits in a waveguide have long-range interactions mediated by photons that cause the emergence of collective states. Destructive interference between the qubits decouples the collective dark states from the waveguide environment. Their inability to emit photons into the waveguide render dark states a valuable resource for preparing long-lived quantum many-body states and realizing quantum information protocols in open quantum systems. However, they also decouple from fields that drive the waveguide, making manipulation a challenge. Here we show the coherent control of a collective dark state that is realized by controlling the interactions between four superconducting transmon qubits and local drives. The dark state's protection against decoherence results in decay times that exceed those of the waveguide-limited single qubits by more than two orders of magnitude. Moreover, we perform a phase-sensitive spectroscopy of the two-excitation manifold and reveal bosonic many-body statistics in the transmon array. Our dark-state qubit provides a starting point for implementing quantum information protocols with collective states.

Waveguide quantum electrodynamics (QED) has become a very active research field to study localized quantum emitters that are coupled to one-dimensional photonic channels. The platform offers novel opportunities to study interacting quantum systems and promises various applications in quantum information processing based on the fundamental physics of light–matter interaction[1]. Typical realizations include natural and artificial atoms, such as superconducting qubits and quantum dots, coupled to optical or microwave waveguides[2–7]. Well-developed control techniques and the possibility to engineer very high coupling efficiencies make superconducting qubits an excellent platform to study waveguide-mediated interactions between multiple emitters. The engineering capabilities of superconducting qubits led to the observation of a broad range of quantum optical phenomena such as the Mollow triplet[7], ultrastrong coupling[8], generation of non-classical photonic states[9,10], qubit–photon bound states[11], topological physics[12] and collective effects[13,14].

Collective states appear in waveguide QED as a result of waveguide-mediated interactions[13,15] and interference effects in an ensemble of emitters[16]. The relative phase between individual emitters determines whether the collective state obtains a sub- or super-radiant decay rate, that is, whether it becomes a dark or bright state. Collective bright states have been measured in various waveguide QED systems[5,13,17–19], whereas dark states have only been spectroscopically observed in superconducting waveguide QED[13,20]. More recently, a multi-qubit dark state has been used to build a microwave cavity[14]; however, full coherent control of the dark state has not been achieved yet. Multi-qubit dark and bright states provide a possibility to investigate the dynamics of interacting quantum systems[21,22], study many-body localization in disordered arrays[23,24] or even build a quantum computation and simulation platform[25] within an open quantum system. A key element to realize these concepts is coherent control of the system. The difficulty of controlling a dark state arises from its main property—it decouples from the electromagnetic environment of the waveguide. In addition, coherent control requires accurate knowledge of the energy and decay characteristics beyond the one-excitation manifold. However, higher-excited states of collective systems have been barely explored so far[26].

In this work, we realize a collective dark state by exploiting near-field and waveguide-mediated interactions between four superconducting transmon qubits. The collective dark state is coherently controlled via two physically separate drive ports, which allows the adjustment of their relative phase and thus solve the problem of driving a state that is decoupled from the waveguide. By tuning the qubits to the decoherence-free frequency, we demonstrate long coherence times along with full coherent control in an open quantum system. We utilize the state-dependent scattering of the collective bright transition to read out the ground- and dark-state populations.

Further, we perform a pulsed spectroscopy to characterize the collective two-excitation states and demonstrate the use of super-radiant transitions to reset the dark-state qubit. Remarkably, when a transmon array has two or more excitations, their bosonic statistics become crucial for the energy spectrum. Our theoretical and experimental analysis show that this leads to collective high-excitation states that are fundamentally different from those of two-level arrays[14,18].

Superconducting qubits can be coupled to a microwave transmission line, much like a natural atom to a nanophotonic fibre or photonic-crystal waveguide (Fig. 1a). The qubit decoherence rate $\Gamma=(\gamma+\gamma_{\mathrm{nr}})/2+\gamma_\phi$ is a sum of radiative decay γ into the waveguide modes, non-radiative energy loss γ_{nr} and pure dephasing γ_ϕ (refs. [27–29]). When the qubit is coupled to a waveguide, the linewidth can be extracted in scattering experiments by measuring the waveguide transmission or reflection, to obtain the coupling strength to the waveguide γ and the non-radiative decoherence rate $\gamma'_{\mathrm{nr}}=\gamma_{\mathrm{nr}}/2+\gamma_\phi$.

---

[1]Institute for Experimental Physics, University of Innsbruck, Innsbruck, Austria. [2]Institute for Quantum Optics and Quantum Information, Austrian Academy of Sciences, Innsbruck, Austria. [3]Nano and Molecular Systems Research Unit, University of Oulu, Oulu, Finland. [4]Institut Quantique and Département de Physique, Université de Sherbrooke, Sherbrooke, Québec, Canada. ✉e-mail: maximilian.zanner@uibk.ac.at

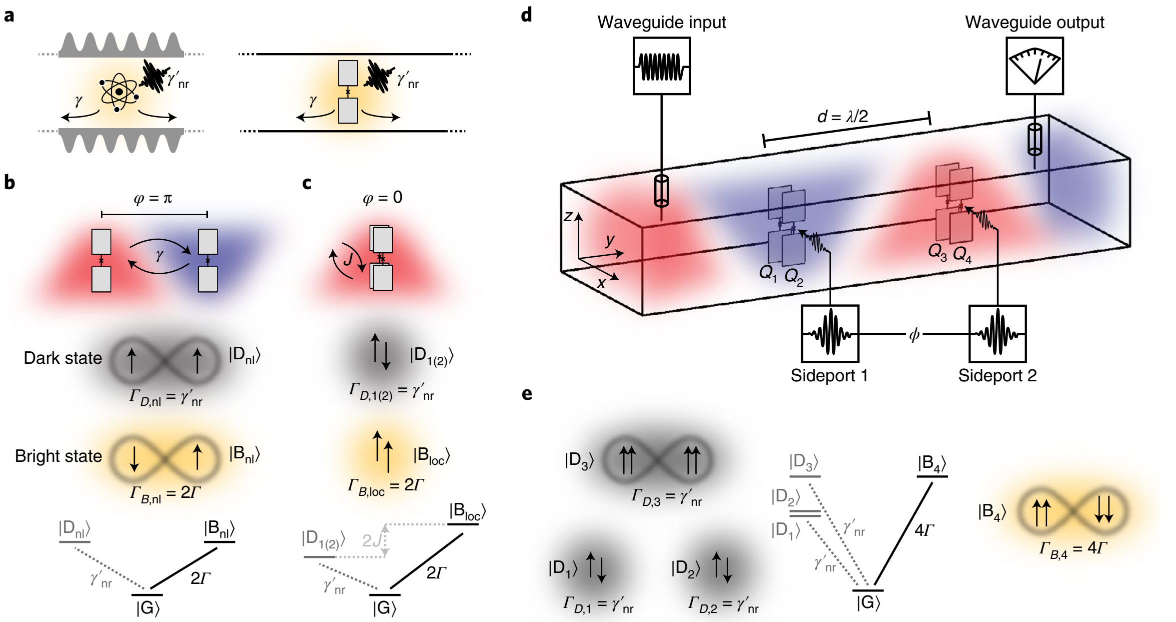

Fig. 1 | Collective states in waveguide QED. a, Decoherence rate $\Gamma = \gamma/2 + \gamma'_{\rm nr}$ of a quantum emitter coupled to a waveguide is given by radiative coupling γ and non-radiative decoherence rate $\gamma'_{\rm nr}$. For waveguide-mediated interactions, it is important to reach the strong coupling limit ($\gamma \gg \gamma'_{\rm nr}$). Left, realizing strong coupling of a natural atom to a photonic waveguide is difficult due to its small dipole moment. Right, a transmon qubit acts as an artificial atom and can be strongly coupled to a microwave waveguide. **b**, For two identical qubits with ground state $|g\rangle$ and first excited state $|e\rangle$ that are separated by $d = \lambda/2$, the phase difference between the qubit locations is π; thus, the non-local dark state $|{\rm D_{nl}}\rangle = (|eg\rangle + |ge\rangle)/\sqrt{2}$ is a symmetric superposition state and the bright state $|{\rm B_{nl}}\rangle = (|eg\rangle - |ge\rangle)/\sqrt{2}$ is an antisymmetric superposition state, illustrated by the in-phase and out-of-phase oscillating transition dipole moments (arrows). The one-excitation state manifold at the bottom shows that both transition energies are degenerate but the states exhibit different decay properties. The dark state is isolated from the waveguide environment and therefore limited to internal losses $\gamma'_{\rm nr}$, whereas the bright-state decoherence rate is enhanced to 2Γ. **c**, Two directly coupled qubits that are located at the same position in the waveguide, that is, $\varphi = 0$, form an antisymmetric dark state $|{\rm D}_{1(2)}\rangle = (|eg\rangle - |ge\rangle)/\sqrt{2}$ and a symmetric bright state $|{\rm B_{loc}}\rangle = (|eg\rangle + |ge\rangle)/\sqrt{2}$. In contrast to waveguide-mediated coupling, the energy degeneracy of the bright and dark states is lifted by the coherent exchange coupling rate $2J$. **d**, Schematic of the full setup. Two pairs of transmon qubits are separated by an effective distance $d = \lambda/2$, combining direct coupling and waveguide-mediated interaction. The ports in the sidewall of the waveguide (sideports 1 and 2) enable the driving of the dark states. **e**, Waveguide-mediated interactions and capacitive couplings between two transmons form the four-qubit one-excitation state manifold. It consists of dark state $|{\rm D_3}\rangle$ and bright state $|{\rm B_4}\rangle$ with decay rate 4Γ, as well as pairwise dark states $|{\rm D_1}\rangle$, $|{\rm D_2}\rangle$ that are localized at the sites and do not interact with the waveguide or the other pair.

The device sketched in Fig. 1d comprises four frequency-tunable transmon qubits[30] acting as artificial atoms. Transmons Q_1 and Q_2 are located on the left, closer to the input side of the waveguide. Transmons Q_3 and Q_4 are located on the right, closer to the output of the waveguide, such that the physical separation between the pairs is $d_y = (46.0 \pm 0.5)$ mm. Within the pairs, the transmons are separated by $d_x = (1.0 \pm 0.2)$ mm, which sets the capacitive coupling strengths J_{12} and J_{34}. The fundamental waveguide mode TE_{10} has a cutoff frequency of $\omega_c/2\pi = 6.55$ GHz (ref. [31]) and its electrical field is polarized parallel to the dipole moment of the transmons such that they efficiently couple to the waveguide. Four superconducting coils can individually control the resonance frequency of all the transmons, such that if only a subset of transmons is used for the experiment, the others are tuned below the waveguide cutoff. More details on the physical construction can be found in Supplementary Sections 1 and 2.

First, we study the case where two transmons interact through the waveguide at a separation $d_y = \lambda/2$ (Fig. 1b). The signal propagating between the transmons acquires a phase $\varphi = 2\pi d_y/\lambda$ that depends on the wavelength $\lambda = 2\pi v/\omega$ and distance d_y, where v is the group velocity in the waveguide and ω is the angular frequency of the wave. Analytically, a phase difference of $\varphi = \pi$ for our setup corresponds to an emission frequency $\omega_\pi/2\pi = (7.312 \pm 0.016)$ GHz, where the uncertainty comes from the alignment error. Here, correlated decay into the waveguide $\gamma_{j,k} = \sqrt{\gamma_j \gamma_k}\cos(\varphi)$ is maximized[15] and coherent waveguide-mediated interaction $\tilde{J}_{j,k} = \sqrt{\gamma_j \gamma_k}\sin(\varphi)/2$ is absent, due to the counter-periodic behaviour. Moreover, the individual waveguide coupling rates are denoted by γ_j and γ_k for transmons $j \neq k$. The photon-mediated interaction leads to symmetric and antisymmetric states under qubit exchange, that is, the dark state $|{\rm D_{nl}}\rangle = (|ge\rangle + |eg\rangle)/\sqrt{2}$ and bright state $|{\rm B_{nl}}\rangle = (|ge\rangle - |eg\rangle)/\sqrt{2}$. For a distance of $\lambda/2$, the phase relation of the electromagnetic field in the waveguide is antisymmetric ($\varphi = \pi$); thus, we can only excite the antisymmetric bright state. The dark-state symmetry is opposite to the field symmetry of the waveguide, eliminating the coupling to the drive field and decay into the waveguide.

Two nearby transmons are directly coupled through the capacitance between the metallic pads of their antennae. Unlike interactions mediated by the waveguide, the capacitive coupling for transmons in this configuration has an effective $1/r^3$ dependence[32], leading to short-range coupling. On resonance, an excitation can coherently swap between the local transmons, resulting in new eigenstates, particularly a symmetric state $|{\rm B_{loc}}\rangle = (|ge\rangle + |eg\rangle)/\sqrt{2}$ and an antisymmetric state $|{\rm D}_{1(2)}\rangle = (|ge\rangle - |eg\rangle)/\sqrt{2}$ (Fig. 1c). The capacitively coupled transmons are located at the same position with respect to the propagating field and symmetrically around the centre of the waveguide. Therefore, the phase of the electrical field is the same for both transmons $\varphi = 0$ and the drive along the waveguide can only access the symmetric state, in contrast to the scenario where the qubits are separated by $\lambda/2$.

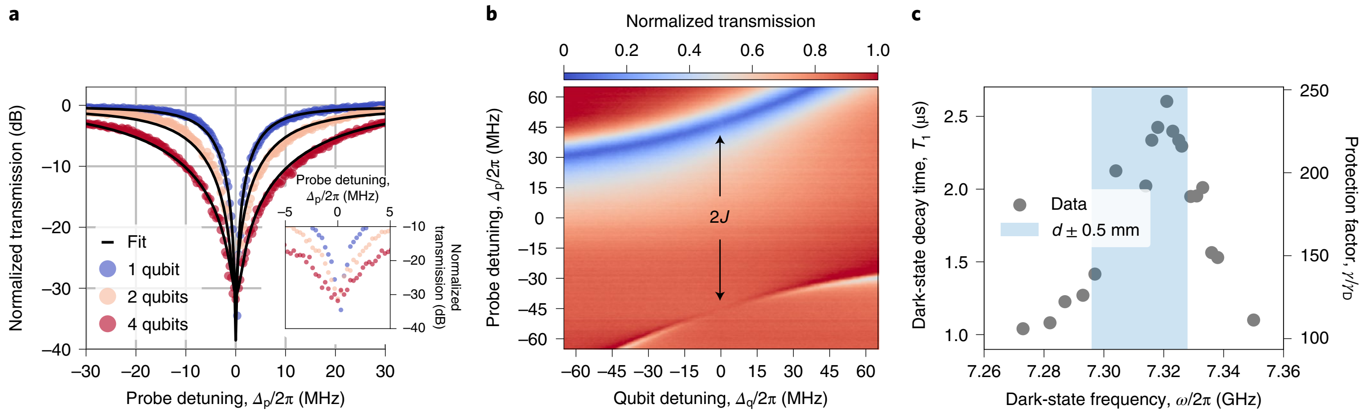

Fig. 2 | Measuring dark and bright states. a, Waveguide transmission as a function of probe frequency around the resonance of the single qubit or the common bright state of the hybridized two- and four-transmon systems. The single qubit linewidth $\Gamma/2\pi=14.9$ MHz increases to $\Gamma_B/2\pi=30.2$ MHz for the two-qubit (local or non-local) bright state and to $\Gamma_{B,4}/2\pi=60.9$ MHz for the four-qubit bright state corresponding to super-radiant transitions. The inset shows a zoomed-in view of the centre of the resonances. **b**, Waveguide transmission as a function of qubit and probe detuning. Two-transmon qubits Q_3 and Q_4 (equivalent for Q_1 and Q_2, respectively; not shown) are tuned in and out of resonance as the transmission is measured through the waveguide for different frequencies. The upper branch yields twice the linewidth $\Gamma_{B,\mathrm{loc}}=2\Gamma$, whereas the lower branch disappears from the transmission, effectively decoupling the transition from the waveguide and reducing the dark-state decay rate to non-radiative losses $\Gamma_{D,1(2)}=\gamma'_{\mathrm{nr}}$. **c**, Dark-state lifetime for a $\lambda/2$-separated transmon pair (here Q_1 and Q_4) as a function of the dark-state frequency. The frequency for maximal correlated decay $\omega_\pi/2\pi=7.321$ GHz is calibrated by measuring the dark-state decay times around the analytical value for a physical separation of $d_y=(46.0\pm0.5)$ mm (blue region). The correlated decay depends on the physical separation and wavelength. When the frequency fulfills $\lambda/2=2\pi v/\omega$, the dark-state symmetry is optimal; hence, we measure the longest decay time T_1. The right axis shows the ratio between the mean value of the single-transmon coupling rates γ_1,γ_4 and the decay rate of the hybridized dark state $\gamma_D=1/T_1$.

Before tuning all the qubits into resonance, we characterize individual qubit and pairwise couplings. The individual qubit and collective bright-state radiative decay rates are extracted from transmission measurements, using a circle-fit routine[33] on the complex-valued scattering parameters. In Fig. 2a, we show the magnitude of the normalized transmission for a single transmon, as well as for two and four transmons tuned to frequency ω_π. For two and four qubits, we observe the typical broadening of the linewidth, caused by superradiant decay. The capacitively coupled transmon pairs have direct coupling strengths $J_{12}/2\pi=43$ MHz and $J_{34}/2\pi=47$ MHz, which can be extracted from an avoided crossing (shown for Q_3 and Q_4; Fig. 2b). The difference in coupling strengths is a result of imperfections in the alignment and machining imprecision, which lifts the degeneracy between the local dark states $|\mathrm{D}_1\rangle$ and $|\mathrm{D}_2\rangle$. The coherent exchange interaction lifts the degeneracy of $|\mathrm{B}_{\mathrm{loc}}\rangle$ and $|\mathrm{D}_{1(2)}\rangle$ and allows us to observe the decoupling of the dark state when we tune the qubits into resonance.

We calibrate the decoherence-free frequency ω_π using the dark state formed by two distant transmons. To control the dark states, we introduce two sideports that are weakly coupled to the local transmon pairs (Fig. 1d). For over a decade, individual drive ports have been applied in on-chip circuit QED experiments[34] that we adapted and implemented in three-dimensional waveguides. In our experiment, we capitalize on the symmetry between the four qubits and sideport drives. The sideports provide an amplitude gradient over the local pairs to access the dark states $|\mathrm{D}_{1(2)}\rangle$, but also the possibility to independently adjust the relative phase ϕ between the local pairs, which allows us to apply a symmetric drive and access the non-local dark state $|\mathrm{D}_{\mathrm{nl}}\rangle$. The field of the drive port does not coincide with the polarization of the TE_{10} waveguide mode and decays exponentially along the propagation direction of the waveguide; thus, the drive is effectively local (Supplementary Section 6).

We measure the ground-state population by employing a state-dependent scattering scheme, adapted from quantum non-demolition state detection in trapped-ion quantum computing[35]. If the collective system is in the ground state $|\mathrm{G}\rangle$, we can coherently scatter photons between the ground state $|\mathrm{G}\rangle$ and superradiant state $|\mathrm{B}_{\mathrm{nl}}\rangle$, which reduces the transmission through the waveguide (Fig. 2a). If the dark state $|\mathrm{D}_{\mathrm{nl}}\rangle$ is populated, the microwave signal is not scattered, resulting in unit transmission. By selectively exciting the dark state using microwave signals applied through the sideports with $\phi=0$, we can experimentally search for the longest dark-state relaxation time around the analytical decoherence-free frequency and indeed find it within the uncertainty at $\omega_\pi/2\pi=7.321$ GHz (Fig. 2c).

From now on, we consider the full system; therefore, we tune all the four transmons into resonance such that the bright transitions of the capacitively coupled pairs match the decoherence-free frequency ω_π. Both local two-qubit bright states interact via the waveguide and create the collective four-qubit states $|\mathrm{B}_4\rangle$ and $|\mathrm{D}_3\rangle$, whereas the local two-qubit dark states $|\mathrm{D}_1\rangle$ and $|\mathrm{D}_2\rangle$ cannot interact via the waveguide. These four states span the first excitation manifold (Fig. 1e). In Fig. 2a, we extract the linewidth $\Gamma_{B,4}/2\pi=60.9$ Mhz resulting from the constructive interference of all the transmons, namely, $\Gamma_{B,4}=\sum_j \Gamma_j$.

To characterize the dark state, we study the time-resolved dynamics. When driving the transmon array through the sideports, the transition amplitudes from the ground state to non-local dark and bright states depend on the driving phase ϕ as

$$|\mathrm{G}\rangle \to |\mathrm{D}_3\rangle : \quad \frac{\hbar\Omega}{2}\left(1+\mathrm{e}^{\mathrm{i}\phi}\right), \tag{1}$$

$$|\mathrm{G}\rangle \to |\mathrm{B}_4\rangle : \quad \frac{\hbar\Omega}{2}\left(1-\mathrm{e}^{\mathrm{i}\phi}\right). \tag{2}$$

Rabi oscillations between $|\mathrm{G}\rangle$ and $|\mathrm{D}_3\rangle$ are shown in Fig. 3a when the amplitude of the drive field Ω is increased and the phase difference between the sideports matches $\phi=2n\pi$ ($n\in\mathbb{Z}$). For an antisymmetric drive with odd integer multiple $\phi=(2n-1)\pi$, we only drive the bright state $|\mathrm{B}_4\rangle$ that decays very rapidly to the ground

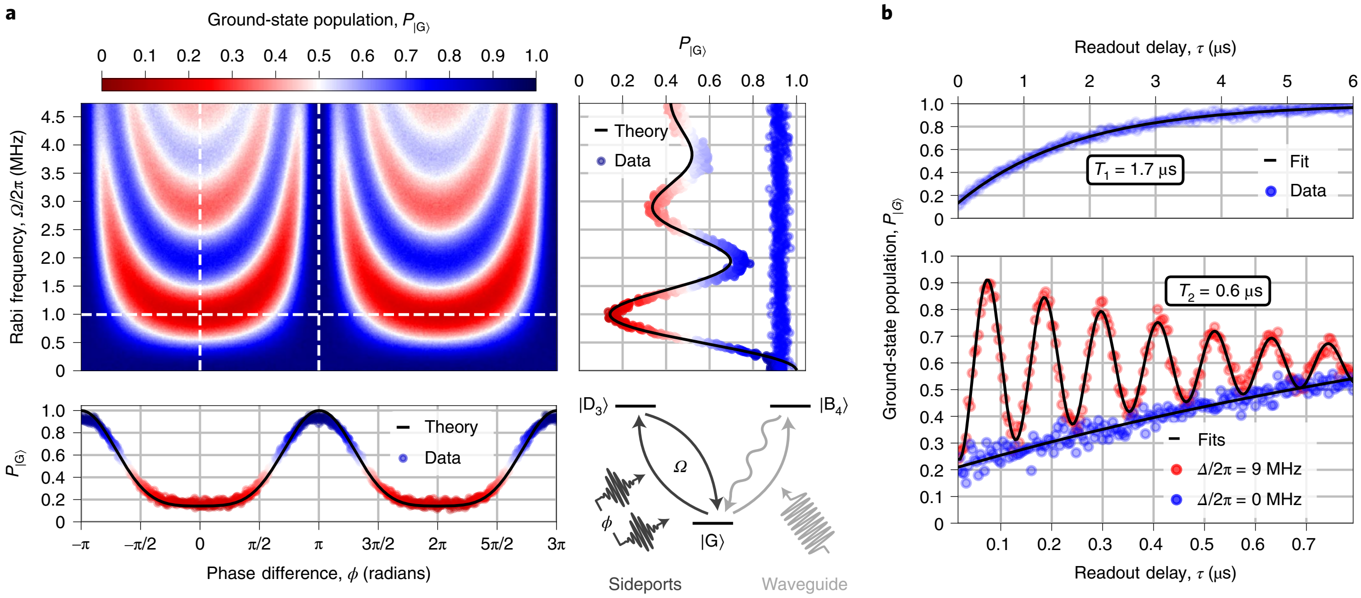

Fig. 3 | Coherent control of the dark state. a, We apply a Gaussian-shaped pulse of total length $t = 240$ ns and standard deviation $\sigma = 40$ ns to observe Rabi oscillation between the ground state $|G\rangle$ and non-local four-qubit dark state $|D_3\rangle$ as a function of Rabi frequency Ω and sideport phase difference ϕ. By applying the pulse through the sideports, we can independently set the phase ϕ. The ground-state population is read out by sending a 5-μs-long rectangular pulse through the waveguide, resonant with the transition between states $|G\rangle$ and $|B_4\rangle$. The right panel shows a vertical linecut at the white dashed lines of the colour map for phase difference $\phi = 0$ and $\phi = \pi$. The bottom panel shows a horizontal linecut for a Rabi frequency of $\Omega/2\pi = 1$ MHz. For the theory curve, we simulate the Hamiltonian (equation (3)) and master equation in Supplementary Information with the parameters specified in Supplementary Table 1. **b**, A symmetric excitation pulse with Rabi frequency $\Omega/2\pi = 1$ MHz and relative phase difference $\phi = 0$ between both sideports is used to populate the collective dark state $|D_3\rangle$. After a variable delay time, the ground-state population is read out to find an average relaxation time $T_1 = (1.71 \pm 0.06)$ μs. In a Ramsey experiment, we find an average coherence time of $T_2 = (0.58 \pm 0.06)$ μs. On resonance ($\Delta/2\pi = 0$), we observe an exponential decay; for a detuned pulse ($\Delta/2\pi = 9$ MHz), we induce oscillations with frequencies corresponding to detuning between the drive frequency and transition frequency between states $|G\rangle$ and $|D_3\rangle$.

state with rate $\Gamma_{B,4}$. Again, we employ the state-dependent scattering readout scheme as for the two-qubit case, now using transition $|G\rangle$ to $|B_4\rangle$ to scatter the waveguide photons. To determine the ground-state population, we conduct a reference measurement of the transmitted readout pulse for the case where all the transmons are tuned below the waveguide cutoff frequency.

With a calibrated π and π/2 pulse, we can investigate the coherence properties of the dark state. For the collective dark state, we measure an average relaxation time $T_1 = (1.71 \pm 0.06)$ μs and coherence time $T_2 = (0.58 \pm 0.06)$ μs (Fig. 3b). In this system, dephasing and frequency fluctuations of the individual qubits cause imperfections in the dark-state symmetry. This results in a finite decay rate into the waveguide; thus, the dark-state relaxation time T_1 depends on the pure transmon dephasing rate γ_ϕ (Supplementary Section 4).

To simulate the collective dynamics shown by the black lines in Fig. 3a, we model the transmons and their direct couplings with the Hamiltonian[26,36,37]

$$\begin{aligned}\hat{H}_{\mathrm{T}}/\hbar &= \sum_{j=1}^{4}\left[\omega_j\hat{n}_j - \frac{U_j}{2}\hat{n}_j(\hat{n}_j-1)\right]\\ &\quad + J_{12}\left(\hat{a}_1^{\dagger}\hat{a}_2 + \mathrm{h.c.}\right) + J_{34}\left(\hat{a}_3^{\dagger}\hat{a}_4 + \mathrm{h.c.}\right),\end{aligned} \tag{3}$$

where ħ is the reduced Planck constant, ω_j is the fundamental resonance frequency and U_j is the anharmonicity of the individual transmon. Operators $\hat{a}_j$ and $\hat{a}_j^{\dagger}$ are the bosonic annihilation and creation operators of the jth transmon and $\hat{n}_j = \hat{a}_j^{\dagger}\hat{a}_j$ is the corresponding number operator. In the presence of the waveguide radiation field, the dynamics are governed by a master equation[14,15] taking into account the coherent exchange interaction $\tilde{J}_{j,k}$ and correlated decay $\gamma_{j,k}$ between the transmons at sites j and k. The properties of the system are then described by the effective non-Hermitian Hamiltonian

$$\begin{aligned}\hat{H}_{\mathrm{eff}}/\hbar &= \hat{H}_{\mathrm{T}}/\hbar + \sum_{jk}\left(\tilde{J}_{j,k} - \frac{i\gamma_{j,k}}{2}\right)\hat{a}_k^{\dagger}\hat{a}_j\\ &\quad - \frac{i}{2}\sum_{j}\gamma_{\mathrm{nr}}\hat{a}_j^{\dagger}\hat{a}_j,\end{aligned} \tag{4}$$

where parameter γ_{nr} describes the non-radiative dissipation of individual transmons, whereas we neglect pure dephasing for simplicity.

As shown in Fig. 3a, the Rabi oscillations decay for large drive amplitudes. This is caused by leakage into fast decaying states of the higher-excitation manifold. To study this in more detail, we explore the two-excitation manifold of the collective four-transmon system (Fig. 4) by concatenating a spectroscopy pulse after populating the dark state $|D_3\rangle$. For the spectroscopy, we change the frequency and relative phase to unveil the symmetry and energy of the states in the two-excitation manifold. When the spectroscopy pulse is resonant with a transition, for example, $|W_5\rangle$, $|W_6\rangle$, $|B_{13}\rangle$ or $|B_{14}\rangle$, the system is reset to the ground state due to the rapid decay of these states dominantly via the bright state $|B_4\rangle$. We denote the collective states by $|D_i\rangle$, $|B_i\rangle$ and $|W_i\rangle$, where the letter refers to their waveguide radiation characteristics, namely, dark, bright or weakly radiant, respectively. The subscript is an ascending enumeration based on their energy value. In Fig. 4, the collectiveness of these states is apparent in the phase dependence of the measured ground-state population (left), which is consistent with the simulation (right) of the model Hamiltonian (equation (4)).

It is essential to note that a transmon is a bosonic multilevel system with anharmonicity U. The many-body excited-state

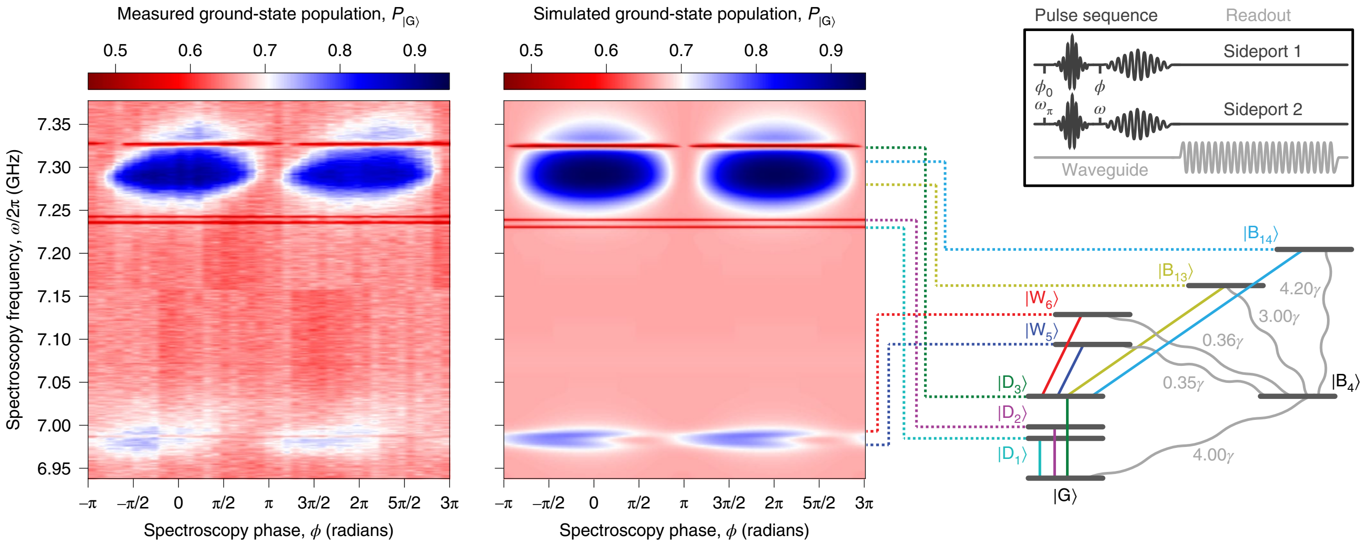

Fig. 4 | Phase-sensitive spectroscopy of the two-excitation manifold. Top right, pulse sequence where we apply a Gaussian-shaped π pulse that populates the dark state $|D_3\rangle$, where the relative phase on the sideports is set to $\phi_0 = 0$ and the frequency is set to the decoherence-free frequency ω_π. Then, we concatenate a long spectroscopy pulse of length $t = 1.2\,\mu s$ ($\sigma = 200$ ns) with variable frequency $\omega/2\pi$ and phase ϕ. We record the waveguide transmission with a 5-μs-long rectangular readout pulse to obtain the measured (left) and simulated (right) ground-state population. The states of the two-excitation manifold have to be coupled to the dark state $|D_3\rangle$ and possess a finite decay rate to the bright state $|B_4\rangle$, which then decays to the ground state $|G\rangle$. Therefore, we measure a high ground-state population when the spectroscopy pulse is resonant with a transition that can be driven from $|D_3\rangle$. The ability to drive the collective states depends on the spectroscopy phase, whereas local states can be driven with any phase. There are six other states in the two-excitation manifold that are not visible in the spectroscopy since they cannot be driven from the dark state $|D_3\rangle$ or do not decay to the bright state $|B_4\rangle$. The parameters for the simulation are given in Supplementary Table 1. To observe the local dark states $|D_{1,2}\rangle$ in the simulation, we have included an amplitude gradient of the local drives, such that the power on transmons Q_2 and Q_4 is three-quarter that on Q_1 and Q_3. This asymmetry produces an additional driving term that is always antisymmetric with respect to the exchange of transmons within the pair. These states do not show a phase dependence as they are only coupled to one drive port. During the time of the spectroscopy pulse, which is of the same order as the lifetime of $|D_3\rangle$, a part of the population decays to the ground state. As a consequence, the phase-sensitive transition between states $|G\rangle$ and $|D_3\rangle$ is visible.

manifolds in bosonic systems are fundamentally different from those of two-level emitters. For example, in our case of four transmons, the two-excitation manifold includes ten basis states, whereas two-level emitters would only have six states. The importance to differentiate between two-level systems and transmons increases with the total excitation number. Here the additional states are the doubly excited states of the transmons, which make an important contribution to the collective superposition states $|W_{5(6)}\rangle$ and $|B_{(13)14}\rangle$ (Fig. 4). States $|W_5\rangle$ and $|W_6\rangle$ are unique to bosonic systems, as they are strongly affected by the negative transmon anharmonicites and are not reproducible by considering two-level systems[38]. In general, in bosonic waveguide QED systems, the number of bright and dark states is higher and the bright states are brighter compared to the case of two-level emitters. The reason is a larger and more versatile many-body Hilbert space[38].

The spectroscopy data in Fig. 4 shows that the transitions $|D_3\rangle$ to $|B_{13}\rangle$ and $|B_{14}\rangle$ not only overlap with the transition of the dark-state qubit $|G\rangle$ to $|D_3\rangle$ but also share the same phase condition on the drive. Consequently, we attribute the damping of the Rabi oscillations in Fig. 3a to the population of these states as we increase the drive amplitude. Remarkably, this leakage effect can be dramatically reduced by increasing the coupling to the waveguide so much that the unwanted excitation to this state can be adiabatically eliminated[39]. Ideally, increasing the waveguide coupling does not affect the coherence and lifetime of the dark state; only the states outside the decoherence-free subspace decay faster. In contrast to conventional solid-state qubits, a symmetry-engineered multi-qubit system makes it possible to independently control the decay properties of the leakage states of the computational states (Supplementary Section 4 and 5).

In conclusion, the experiment demonstrates that collective dark states constitute a resource for coherent quantum information and can be controlled by local drives with an adjustable phase relation. The collective four-transmon system comprises a one-excitation state manifold with long-lived dark states, as well as one rapidly decaying bright state. In particular, we achieve an effective protection from the waveguide, leading to a decrease in the relaxation rate by a factor of 160 compared with the single-qubit coupling rate or a factor of 650 compared with the collective bright state. The degenerate bright state can be used to read out the system. Although in conventional resonator-based architectures, detuning between the readout cavity and qubit plays an important role for its coherence time, the experiment shows that the protection can be engineered by taking into account the symmetry properties of the system as both transitions are resonant. Unlike in previous experiments, the observation of the weakly radiant states $|W_5\rangle$ and $|W_6\rangle$ is a direct manifestation of the transmons' bosonic nature and demonstrates the necessity to go beyond the two-level approximation when trying to engineer many-body physics with artificial atoms[38].

Looking forward, coherent control of multi-qubit dark states opens up the possibility to investigate the dynamics of interacting quantum many-body systems[21,22], to study many-body localization in disordered arrays[23,24] or even realize a quantum computation and simulation platform within an open quantum system[25]. On one hand, the adiabatic elimination of higher-excited states promises the possibility to further optimize the coherent control of the dark state; on the other hand, the two-excitation manifold can be used to reset the dark-state qubit and transfer quantum information into itinerant photons. This mechanism is a source of cluster-state creation[40], whereas the cascaded decay can be utilized to study entanglement between photons of different frequencies. Finally, the interplay between long-lived subradiant states and weakly radiative states can give new insights into incoherent scattering properties and photon–photon correlations[41–46].

Online content

Any methods, additional references, Nature Research reporting summaries, source data, extended data, supplementary information, acknowledgements, peer review information; details of author contributions and competing interests; and statements of data and code availability are available at https://doi.org/10.1038/s41567-022-01527-w.

Received: 9 June 2021; Accepted: 25 January 2022;

References

1. Sheremet, A. S., Petrov, M. I., Iorsh, I. V., Poshakinskiy, A. V. & Poddubny, A. N. Waveguide quantum electrodynamics: collective radiance and photon-photon correlations. Preprint at https://arxiv.org/abs/2103.06824 (2021).
2. Roy, D., Wilson, C. M. & Firstenberg, O. Colloquium: strongly interacting photons in one-dimensional continuum. *Rev. Mod. Phys.* **89**, 021001 (2017).
3. Masson, S. J. & Asenjo-Garcia, A. Atomic-waveguide quantum electrodynamics. *Phys. Rev. Research* **2**, 043213 (2020).
4. Goban, A. et al. Atom–light interactions in photonic crystals. *Nat. Commun.* **5**, 3808 (2014).
5. Corzo, N. V. et al. Large Bragg reflection from one-dimensional chains of trapped atoms near a nanoscale waveguide. *Phys. Rev. Lett.* **117**, 133603 (2016).
6. Lodahl, P., Mahmoodian, S. & Stobbe, S. Interfacing single photons and single quantum dots with photonic nanostructures. *Rev. Mod. Phys.* **87**, 347 (2015).
7. Astafiev, O. et al. Resonance fluorescence of a single artificial atom. *Science* **327**, 840–843 (2010).
8. Forn-Díaz, P. et al. Ultrastrong coupling of a single artificial atom to an electromagnetic continuum in the nonperturbative regime. *Nat. Phys.* **13**, 39–43 (2017).
9. Hoi, I.-C. et al. Generation of nonclassical microwave states using an artificial atom in 1D open space. *Phys. Rev. Lett.* **108**, 263601 (2012).
10. Kannan, B. et al. Generating spatially entangled itinerant photons with waveguide quantum electrodynamics. *Sci. Adv.* **6**, eabb8780 (2020).
11. Sundaresan, N. M., Lundgren, R., Zhu, G., Gorshkov, A. V. & Houck, A. A. Interacting qubit-photon bound states with superconducting circuits. *Phys. Rev. X* **9**, 011021 (2019).
12. Kim, E. et al. Quantum electrodynamics in a topological waveguide. *Phys. Rev. X* **11**, 011015 (2021).
13. van Loo, A. F. et al. Photon-mediated interactions between distant artificial atoms. *Science* **342**, 1494–1496 (2013).
14. Mirhosseini, M. et al. Cavity quantum electrodynamics with atom-like mirrors. *Nature* **569**, 692–697 (2019).
15. Lalumière, K. et al. Input-output theory for waveguide QED with an ensemble of inhomogeneous atoms. *Phys. Rev. A* **88**, 043806 (2013).
16. Goban, A. et al. Superradiance for atoms trapped along a photonic crystal waveguide. *Phys. Rev. Lett.* **115**, 063601 (2015).
17. Kim, J.-H., Aghaeimeibodi, S., Richardson, C. J. K., Leavitt, R. P. & Waks, E. Super-radiant emission from quantum dots in a nanophotonic waveguide. *Nano Lett.* **18**, 4734–4740 (2018).
18. Mlynek, J. A., Abdumalikov, A. A., Eichler, C. & Wallraff, A. Observation of Dicke superradiance for two artificial atoms in a cavity with high decay rate. *Nat. Commun.* **5**, 5186 (2014).
19. Rosario Hamann, A. et al. Nonreciprocity realized with quantum nonlinearity. *Phys. Rev. Lett.* **121**, 123601 (2018).
20. Brehm, J. D. et al. Waveguide bandgap engineering with an array of superconducting qubits. *npj Quantum Mater.* **6**, 10 (2021).
21. González-Tudela, A., Paulisch, V., Chang, D. E., Kimble, H. J. & Cirac, J. I. Deterministic generation of arbitrary photonic states assisted by dissipation. *Phys. Rev. Lett.* **115**, 163603 (2015).
22. Albrecht, A., Henriet, L., Asenjo-Garcia, A., Dieterle, P. B., Painter, O. & Chang, D. E. Subradiant states of quantum bits coupled to a one-dimensional waveguide. *New J. Phys.* **21**, 025003 (2019).
23. Orell, T., Michailidis, A. A., Serbyn, M. & Silveri, M. Probing the many-body localization phase transition with superconducting circuits. *Phys. Rev. B* **100**, 134504 (2019).
24. Fayard, N., Henriet, L., Asenjo-Garcia, A. & Chang, D. E. Many-body localization in waveguide quantum electrodynamics. *Phys. Rev. Research* **3**, 033233 (2021).
25. Paulisch, V., Kimble, H. J. & González-Tudela, A. Universal quantum computation in waveguide QED using decoherence free subspaces. *New J. Phys.* **18**, 043041 (2016).
26. Hacohen-Gourgy, S., Ramasesh, V. V., De Grandi, C., Siddiqi, I. & Girvin, S. M. Cooling and autonomous feedback in a Bose-Hubbard chain with attractive interactions. *Phys. Rev. Lett.* **115**, 240501 (2015).
27. Lu, Y. et al. Characterizing decoherence rates of a superconducting qubit by direct microwave scattering. *npj Quantum Inf.* **7**, 35 (2021).
28. Burnett, J. J. et al. Decoherence benchmarking of superconducting qubits. *npj Quantum Inf.* **5**, 54 (2019).
29. Müller, C., Lisenfeld, J., Shnirman, A. & Poletto, S. Interacting two-level defects as sources of fluctuating high-frequency noise in superconducting circuits. *Phys. Rev. B* **92**, 035442 (2015).
30. Koch, J. et al. Charge-insensitive qubit design derived from the Cooper pair box. *Phys. Rev. A* **76**, 042319 (2007).
31. Pozar, D. M. *Microwave Engineering* 4th edn (Wiley, 2012).
32. Dalmonte, M. et al. Realizing dipolar spin models with arrays of superconducting qubits. *Phys. Rev. B* **92**, 174507 (2015).
33. Probst, S., Song, F. B., Bushev, P. A., Ustinov, A. V. & Weides, M. Efficient and robust analysis of complex scattering data under noise in microwave resonators. *Rev. Sci. Instrum.* **86**, 024706 (2015).
34. Leek, P. J. et al. Cavity quantum electrodynamics with separate photon storage and qubit readout modes. *Phys. Rev. Lett.* **104**, 100504 (2010).
35. Leibfried, D., Blatt, R., Monroe, C. & Wineland, D. Quantum dynamics of single trapped ions. *Rev. Mod. Phys.* **75**, 281 (2003).
36. Roushan, P. et al. Spectroscopic signatures of localization with interacting photons in superconducting qubits. *Science* **358**, 1175–1179 (2017).
37. Ma, R., Saxberg, B., Owens, C., Leung, N., Lu, Y., Simon, J. & Schuster, D. I. A dissipatively stabilized Mott insulator of photons. *Nature* **566**, 51–57 (2019).
38. Orell, T. et al. Collective bosonic effects in an array of transmon devices. Preprint at https://arxiv.org/abs/2112.08134 (2021).
39. Reiter, F. & Sørensen, A. S. Effective operator formalism for open quantum systems. *Phys. Rev. A* **85**, 032111 (2012).
40. Besse, J.-C. et al. Realizing a deterministic source of multipartite-entangled photonic qubits. *Nat. Commun.* **11**, 4877 (2020).
41. Ke, Y., Poshakinskiy, A. V., Lee, C., Kivshar, Y. S. & Poddubny, A. N. Inelastic scattering of photon pairs in qubit arrays with subradiant states. *Phys. Rev. Lett.* **123**, 253601 (2019).
42. Scigliuzzo, M. et al. Primary thermometry of propagating microwaves in the quantum regime. *Phys. Rev. X* **10**, 041054 (2020).
43. Hoi, I.-C. et al. Demonstration of a single-photon router in the microwave regime. *Phys. Rev. Lett.* **107**, 073601 (2011).
44. Brody, D. C. Biorthogonal quantum mechanics. *J. Phys. A: Math. Theor.* **47**, 035305 (2013).
45. Autler, S. H. & Townes, C. H. Stark effect in rapidly varying fields. *Phys. Rev.* **100**, 703 (1955).
46. Barnett, S. and Radmore, P. M. *Methods in Theoretical Quantum Optics* (Oxford Univ. Press, 2002).

Data availability

The data that support the findings of this study are available on Zenodo (https://zenodo.org/record/5772190).

Code availability

The code used for data analysis and simulated results is available from the corresponding author upon reasonable request.

Acknowledgements

We thank A. Strasser for fabricating the waveguide sample. We would like to thank E. I. Rosenthal for valuable comments on the manuscript. M.Z. and S.O. acknowledge funding by the European Research Council (ERC) under the European Union's Horizon 2020 research and innovation programme (714235). M.Z. and C.M.F.S. acknowledge support by the Austrian Science Fund FWF within the DK-ALM (W1259-N27). R.A. acknowledges support from the Austrian Science Fund FWF within the SFB-BeyondC (F7106-N38). T.O. and M.S. acknowledge funding by the Emil Aaltonen Foundation and by the Academy of Finland (316619 and 320086). M.L.J. acknowledges funding from the Canada First Research Excellence Fund.

Author contributions

M.Z. and G.K. conceived and designed the experiment. M.Z. simulated and fabricated the devices and also conducted the measurements. M.Z. and C.M.F.S. analysed the data. T.O. and M.S. developed the theoretical model and performed the simulations. M.Z. and G.K. wrote the manuscript. All the authors discussed the results and contributed to the writing of the manuscript.

Competing interests

The authors declare no competing interests.

Additional information

Supplementary information The online version contains supplementary material available at https://doi.org/10.1038/s41567-022-01527-w.

Correspondence and requests for materials should be addressed to Maximilian Zanner.

Peer review information *Nature Physics* thanks the anonymous reviewers for their contribution to the peer review of this work.

Reprints and permissions information is available at www.nature.com/reprints.